

emitter¹³. However, these sources did not find practical application owing to their very short lifetimes. Because the energy spread of the carbon nanotube emitter^{8,9} of 0.3 eV is smaller than that of a Schottky emitter and is similar to the value of the cold field-emission gun, it is expected that the application of the carbon nanotube source in high-resolution electron-beam instruments will improve the performance of these instruments significantly. In probe-forming electron-beam instruments a trade-off has to be made between the spot size on the one hand and the electron current on the other hand. The first determines the spatial resolution, while the latter determines the time it takes to complete an image. Both aspects will benefit from the carbon nanotube source. Spatial and temporal coherence combined with a large brightness is also very important for transmission electron microscopy, energy-resolved spectroscopy and electron holography. □

Methods

An individual carbon nanotube was mounted on a tungsten tip by using a piezo nanomanipulator (Omicron) in a scanning electron microscope (SEM, Philips) as follows.

Attachment of nanotube to tungsten tip

First, a tungsten wire was welded onto a tungsten heating filament. The wire was electrochemically etched to a moderately sharp tip. This tip was transferred into the SEM and carefully pierced into carbon tape (STR tape from Shinto Paint Co.). The glue applied in this manner on the tip is necessary for a firm attachment of the nanotube.

Next, the main nanotube sample was searched for a suitable tube. The carbon nanotube sample contained multi-walled carbon nanotubes grown with the arc discharge method¹⁹. We chose a long, straight, thin tube that was uniform in diameter, pointed in the direction of the tip and was sufficiently free from other tubes to allow approaching by the tungsten tip. This tube was approached by the tip. When the tip was close enough, the tube stuck to the tip, after which it was further aligned with the axis of the tungsten tip by pulling. The breaking-off of the carbon nanotube is the most difficult part of the procedure. The carbon material is extremely strong and it can only be broken by brute force. Breaking occurs either by Joule heating with a current through the tube of more than 20 μA , or by applying a mechanical force. Each time a nanotube emitter was made, it was tested for emission already in the SEM using a metal foil placed 5 μm in front of the tube and a voltage difference between the tube and the foil of about 60–80 V.

Cleaning of carbon nanotube

An electron emitter prepared in this way was transferred into the pre-vacuum chamber of the ultrahigh vacuum system and 'baked' for half an hour using a halogen light bulb, after which it could enter the ultrahigh vacuum. To obtain a stable emission current, the carbon nanotube had to be cleaned carefully of molecules adsorbed on the tube and impurities in the tube structure. Therefore, the tube was first heated to a temperature of 700 °C for at least 10 min. This temperature is the carbonization temperature, at which volatile species are driven off the tube². The temperature was measured with an infrared pyrometer that was calibrated using a tungsten wire and a thermocouple inside the vacuum system. After the first heating the temperature was reduced to 600 °C and a voltage difference was applied between the emitter and the housing of the vacuum system, such that an emission current of 1 μA was obtained. At first, the emission usually showed large fluctuations, but after about 5 min the current became more stable. Then the emission current was reduced to 100 nA and the emitter was operated for a longer period of time.

Received 8 July; accepted 16 October 2002; doi:10.1038/nature01233.

- Saito, Y. & Uemura, S. Field emission from carbon nanotubes and its application to electron sources. *Carbon* **38**, 169–182 (2000).
- Saito, R., Dresselhaus, G. & Dresselhaus, M. S. *Physical Properties of Carbon Nanotubes* (Imperial College Press, London, 1998).
- Bonard, J. M., Salvétat, J. P., Stockli, T., Forro, L. & Chatelain, A. Field emission from carbon nanotubes: perspectives for applications and clues to the emission mechanism. *Appl. Phys. A* **69**, 245–254 (1999).
- Dean, K. A., von Allmen, P. & Chalamala, B. R. Three behavioral states observed in field emission from single-walled carbon nanotubes. *J. Vac. Sci. Technol. B* **17**, 1959–1969 (1999).
- Purcell, S. T., Vincent, P., Journet, C. & Binh, V. T. Hot nanotubes: stable heating of individual multiwall carbon nanotubes to 2000 K induced by the field-emission current. *Phys. Rev. Lett.* **88**, 105502 (2002).
- Dean, K. A. & Chalamala, B. R. The environmental stability of field emission from single-walled carbon nanotubes. *Appl. Phys. Lett.* **75**, 3017–3019 (1999).
- Fransen, M. J., van Rooy, T. L. & Kruij, P. Field emission energy distributions from individual multiwalled carbon nanotubes. *Appl. Surf. Sci.* **146**, 312–327 (1999).
- Gröning, O., Kuttel, O. M., Emmenegger, C., Gröning, P. & Schlapbach, L. Field emission properties of carbon nanotubes. *J. Vac. Sci. Technol. B* **18**, 665–678 (2000).
- de Jonge, N. & van Druten, N. J. Field emission from individual multiwalled carbon nanotubes prepared in an electron microscope. *Ultramicroscopy* (in the press).
- Hawkes, P. W. & Kasper, E. *Principles of Electron Optics II: Applied Geometrical Optics* (Academic, London, 1996).
- Fransen, M. J. *et al.* Characterization of ultrasharp field emitters by projection microscopy. *Appl. Surf. Sci.* **94/95**, 107–112 (1995).
- Hawkes, P. W. & Kasper, E. *Principles of Electron Optics III: Wave Optics* (Academic, London, 1996).

- Spence, J. C. H., Qian, W. & Silverman, M. P. Electron source brightness and degeneracy from Fresnel fringes in field emission point projection microscopy. *J. Vac. Sci. Technol. A* **12**, 542–547 (1994).
- Schmid, H. & Fink, H. W. Carbon nanotubes are coherent electron sources. *Appl. Phys. Lett.* **70**, 2679–2680 (1997).
- Dean, K. A. & Chalamala, B. R. Field emission microscopy of carbon nanotube caps. *J. Appl. Phys.* **85**, 3832–3836 (1999).
- Saito, Y. *et al.* Conical beams from open nanotubes. *Nature* **389**, 554–555 (1997).
- van Veen, A. H. V., Hagen, C. W., Barth, J. E. & Kruij, P. Reduced brightness of the ZrO/W Schottky electron emitter. *J. Vac. Sci. Technol. B* **19**, 2038–2044 (2001).
- Orloff, J. Survey of electron sources for high-resolution microscopy. *Ultramicroscopy* **28**, 88–97 (1989).
- Colbert, D. T. *et al.* Growth and sintering of fullerene nanotubes. *Science* **266**, 1218–1222 (1994).

Acknowledgements We thank M. Kaiser for the TEM images, N. J. van Druten and B. Buijse for discussions, T. van Rooij for help with the vacuum system and R. E. Smalley for providing the carbon nanotube sample. N.d.J. was supported by FEI company. T.H.O. was supported by Nederlandse organisatie voor wetenschappelijk onderzoek and stichting voor fundamenteel onderzoek der materie.

Competing interests statement The authors declare that they have no competing financial interests.

Correspondence and requests for materials should be addressed to N.J. (e-mail: niels.dejonge@philips.com).

Exchange-coupled nanocomposite magnets by nanoparticle self-assembly

Hao Zeng*†, Jing Li‡, J. P. Liu†, Zhong L. Wang‡ & Shouheng Sun*

* IBM T. J. Watson Research Center, Yorktown Heights, New York 10598, USA
 † Institute for Micromanufacturing, Louisiana Tech University, Ruston, Louisiana 71272, USA
 ‡ School of Materials Science and Engineering, Georgia Institute of Technology, Atlanta, Georgia 30332, USA

Exchange-spring magnets are nanocomposites that are composed of magnetically hard and soft phases that interact by magnetic exchange coupling¹. Such systems are promising for advanced permanent magnetic applications, as they have a large energy product—the combination of permanent magnet field and magnetization—compared to traditional, single-phase materials^{1–3}. Conventional techniques, including melt-spinning^{4–6}, mechanical milling^{7–9} and sputtering^{10–12}, have been explored to prepare exchange-spring magnets. However, the requirement that both the hard and soft phases are controlled at the nanometre scale, to ensure efficient exchange coupling, has posed significant preparation challenges. Here we report the fabrication of exchange-coupled nanocomposites using nanoparticle self-assembly. In this approach, both FePt and Fe₃O₄ particles are incorporated as nanometre-scale building blocks into binary assemblies. Subsequent annealing converts the assembly into FePt–Fe₃Pt nanocomposites, where FePt is a magnetically hard phase and Fe₃Pt a soft phase. An optimum exchange coupling, and therefore an optimum energy product, can be obtained by independently tuning the size and composition of the individual building blocks. We have produced exchange-coupled isotropic FePt–Fe₃Pt nanocomposites with an energy product of 20.1 MJ Oe, which exceeds the theoretical limit of 13 MJ Oe for non-exchange-coupled isotropic FePt by over 50 per cent.

Hexane dispersions of FePt (refs 13, 14) and Fe₃O₄ (ref. 15) nanoparticles with selected concentration, volume and sizes were mixed under ultrasonic agitation, and three-dimensional binary assemblies were induced by either evaporation of the hexane or addition of ethanol. The mass ratio of Fe₃O₄ and FePt was controlled in the range from 1:5 to 1:20, while the size of FePt

was kept at 4 nm and Fe_3O_4 was varied from 4 nm to 12 nm. Figure 1 shows transmission electron microscopy (TEM) images of Fe_3O_4 : $\text{Fe}_{58}\text{Pt}_{42}$ binary assemblies with different sizes and fixed mass ratio of 1:10. Depending on the sizes of nanoparticles, we observed three different assembly structures. For the 4 nm:4 nm assembly (Fig. 1a), $\text{Fe}_{58}\text{Pt}_{42}$ and Fe_3O_4 randomly occupy the sites in a hexagonal lattice; but for the 8 nm:4 nm assembly (Fig. 1b), a typical local ordering appears with each big particle (Fe_3O_4) surrounded by 6–8 small particles ($\text{Fe}_{58}\text{Pt}_{42}$). A large difference in particle sizes in an assembly, such as in a 12 nm:4 nm assembly (Fig. 1c), however, results in clear phase segregation with the 12 nm and 4 nm particles forming their own particle lattice arrays. These ordering structures depend mainly on the particle size ratio, as in the case of Au particle

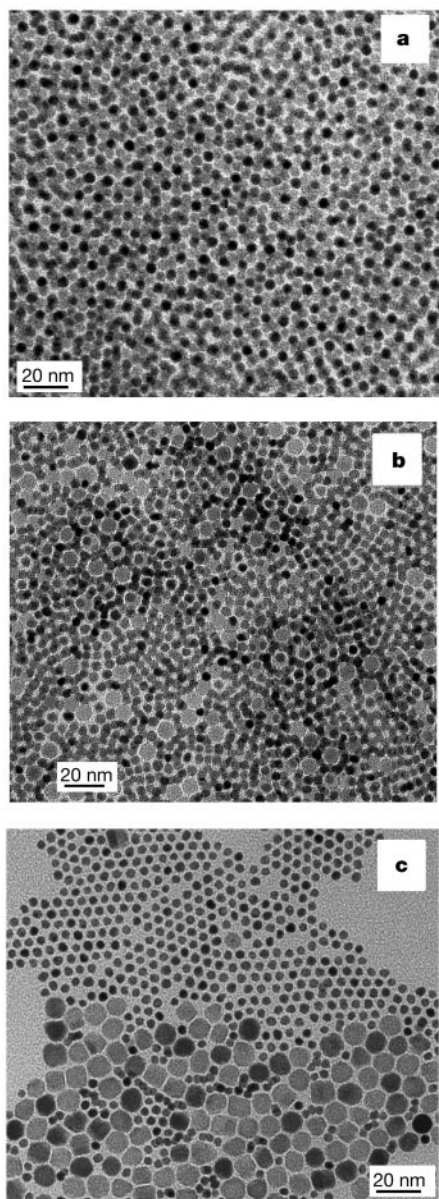


Figure 1 TEM images showing binary nanoparticle assemblies. **a**, Fe_3O_4 (4 nm): $\text{Fe}_{58}\text{Pt}_{42}$ (4 nm) assembly; **b**, Fe_3O_4 (8 nm): $\text{Fe}_{58}\text{Pt}_{42}$ (4 nm) assembly; and **c**, Fe_3O_4 (12 nm): $\text{Fe}_{58}\text{Pt}_{42}$ (4 nm) assembly. The assembly contained Fe_3O_4 and FePt binary nanoparticles with a mass ratio of Fe_3O_4 :FePt = 1/10 and was formed by solvent evaporation of the mixed nanoparticle dispersions on amorphous carbon-coated TEM grids. All images were acquired using a Philips CM12 microscope at 120 kV.

assembly¹⁶, and are insensitive to the mass ratio range we studied.

The binary assemblies were converted into FePt– Fe_3Pt nanocomposites by annealing under a flow of Ar + 5% H_2 at 650 °C for 1 h. The annealing reduces iron oxide to iron¹⁵, and transforms the FePt from disordered face-centred cubic (f.c.c.) to ordered face-centred tetragonal (f.c.t.) structure¹³ that possesses high magnetocrystalline anisotropy ($> 5 \times 10^7 \text{ erg cm}^{-3}$) (refs 17, 18), providing a large coercivity H_c in the nanocomposites. The high temperature treatment under gas flow also desorbs the organic stabilizers around each

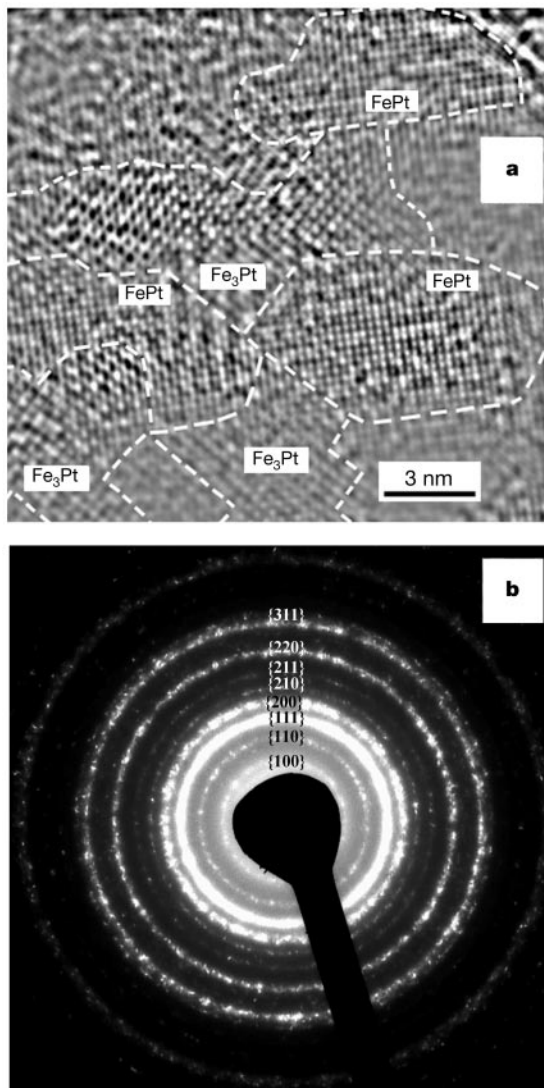


Figure 2 Structural analyses of the FePt– Fe_3Pt nanocomposite obtained from the annealed Fe_3O_4 (4 nm): $\text{Fe}_{58}\text{Pt}_{42}$ (4 nm) assembly. **a**, A typical HRTEM image for a sintered FePt– Fe_3Pt particle. The FePt and Fe_3Pt phases are in coexistence as different domains within the particle, with each domain having a dimension of about 5 nm, showing a modulated FePt– Fe_3Pt spatial distribution. Here, the FePt (ordered f.c.t. structure) and Fe_3Pt (ordered f.c.c. structure) phases were identified by their different [001] projected potential, owing to their different composition modulation periodicities. The image was acquired using a Jeol 4000EX HRTEM at 400 kV. To prepare the TEM samples, the composite was deposited on a solid NaCl substrate. The substrate was then removed in water, and the composite was thinned using ion milling for TEM observation. **b**, A typical SAD pattern of the FePt– Fe_3Pt nanocomposite. The f.c.t.-structured FePt was indexed in the ring pattern. The diffraction rings of the f.c.c.-structured Fe_3Pt cannot be resolved from those of the FePt phase. The ring pattern of the diffraction demonstrates that the nanocrystallites in the nanocomposite are three-dimensionally randomly oriented.

particle, allowing the nanoparticles to sinter. The partial interdiffusion between Fe and FePt creates a new f.c.c.-structured phase, Fe₃Pt, which is magnetically soft with high magnetization¹⁹. Figure 2a is a typical high-resolution TEM (HRTEM) image of a sintered sample obtained from a 4 nm:4 nm assembly. Structural analysis reveals that the coalesced particle is divided into two distinct phases with dimensions of the order of 5 nm: a f.c.c. FePt phase that is magnetically hard, and a f.c.c. Fe₃Pt phase that is magnetically soft. Elemental analysis from spatially resolved energy dispersive spectroscopy (EDS) confirms the existence of two phases with the compositions of Fe:Pt close to 1:1 and 3:1 respectively. After examining various annealed 4 nm:4 nm and 8 nm:4 nm samples with different initial mass ratios, we found that: (1) the Fe₃Pt phase is uniformly dispersed in the FePt matrix; and (2) its dimension is below 10 nm. Figure 2b is a typical selected area diffraction (SAD) pattern of a FePt–Fe₃Pt nanocomposite. The ring pattern in SAD indicates three-dimensional random crystal orientation. The SAD patterns from different tilting angles show similar ring patterns, demonstrating that the isotropic FePt–Fe₃Pt nanocomposite has formed. Trace amounts of α-Fe probably exist in the composite from the 8 nm:4 nm assembly, as suggested by both TEM and EDS analyses, whereas in the annealed 12 nm:4 nm sample, we observe large α-Fe particles over 20 nm in diameter, due to phase segregation observed in the as-prepared sample.

Magnetic properties of FePt–Fe₃Pt nanocomposites vary with different initial mass ratios of Fe₃O₄ and Fe₅₈Pt₄₂. Figure 3 shows the saturation magnetization (M_s), remanent magnetization (M_r) and coercivity (H_c) of the FePt–Fe₃Pt composites from the Fe₃O₄ (4 nm):Fe₅₈Pt₄₂ (4 nm) assemblies as a function of the initial mass ratio, Fe₃O₄:Fe₅₈Pt₄₂. It can be seen that M_s increases monotonically from 950 e.m.u. cm⁻³ for pure FePt to 1,110 e.m.u. cm⁻³ for the 1:5 mass ratio, while H_c decreases sharply from 19 kOe to 6.8 kOe. The M_s of the pure FePt assembly is about 15% lower than the 1,100 e.m.u. cm⁻³ reported for bulk FePt¹⁸. This could result from nanoparticle size, surface and composition effects. M_r shows a maximum of 740 e.m.u. cm⁻³ at the 1:10 mass ratio, a 17% increase from pure FePt. The remanence ratio M_r/M_s values for all samples are greater than 0.6. Figure 4a is a representative hysteresis loop for the composite from the 4 nm:4 nm assembly with 1:10 mass ratio. Although the sample consists of both magnetically hard and soft

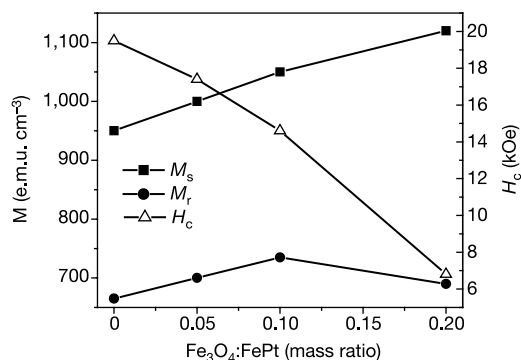


Figure 3 M_s , M_r and H_c of the FePt–Fe₃Pt nanocomposites from the annealed Fe₃O₄ (4 nm):Fe₅₈Pt₄₂ (4 nm) assemblies as a function of mass ratio of Fe₃O₄:FePt. All the data were collected at room temperature on a superconducting quantum interference device (SQUID) magnetometer with field up to 7 T. The magnetic moment is measured as σ (moment per unit mass), and converted to M (moment per unit volume) assuming an ideal density derived from the final Fe and Pt composition of the composite. The elemental composition of the nanocomposite was obtained by inductively coupled plasma–optical emission spectrometry. The impurity level is less than 2%. Because the complete saturation is not reached under a field of up to 7 T, M measured at 7 T is used to represent the lower bound of M_s .

phases, the hysteresis measurements show that the magnetization changes smoothly with field, similar to the hysteresis behaviour of a single-phase material²⁰, indicating that the exchange coupling between the two phases has been realized. The hysteresis measurements also reveal that the remanence of the two-phase nanocomposites is higher than that of the single-phase FePt, which is further evidence of effective hard–soft exchange coupling.

The magnetic behaviour of the FePt–Fe₃Pt nanocomposites changes significantly with the initial sizes of Fe₃O₄ and Fe₅₈Pt₄₂. For the composite from Fe₃O₄ (8 nm):Fe₅₈Pt₄₂ (4 nm) assembly with a mass ratio of 1:10, hysteresis measurements show a single-phase-like loop (not shown here) with large H_c at about 24 kOe and enhanced remanence; but for the composite from Fe₃O₄ (12 nm):Fe₅₈Pt₄₂ (4 nm) assembly with the same mass ratio, the loop shows a kink at low field (Fig. 4b). These changes in hysteresis behaviour correlate directly to size-dependent assembly structures observed in the TEM images (Fig. 1). The Fe₃O₄ (8 nm):Fe₅₈Pt₄₂ (4 nm) assembly possesses a well-mixed structure, with all Fe₃O₄ being surrounded by Fe₅₈Pt₄₂ particles (Fig. 1b). Such a structure leads to a modulated Fe₃Pt soft phase and FePt hard phases in the annealed composite with the soft grains limited to sizes less than 10 nm, as confirmed by HRTEM analyses. For the composite from a Fe₃O₄ (12 nm):Fe₅₈Pt₄₂ (4 nm) assembly, however, due to the spatial segregation of Fe₅₈Pt₄₂ and Fe₃O₄ particles (Fig. 1c), large Fe particles over 20 nm in diameter are formed. For effective exchange coupling to occur within a two-phase magnet, the dimension of the soft phase should be smaller than twice the domain wall width of the hard phase, at about 10 nm (refs 1–3). Therefore, in a composite with a large soft phase, hard and soft phases are not able to switch cooperatively. As a result, its hysteresis loop shows a two-phase behaviour (Fig. 4b).

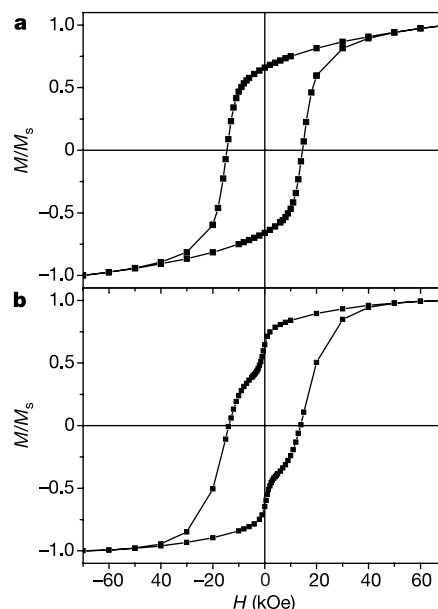


Figure 4 Typical hysteresis loops of two FePt-based nanocomposites. The composites were made from the annealed Fe₃O₄:FePt assemblies with particle mass ratio being kept constantly at Fe₃O₄:FePt = 1:10. **a**, FePt–Fe₃Pt nanocomposite from Fe₃O₄ (4 nm):Fe₅₈Pt₄₂ (4 nm) assembly. The loop shows single-phase-like behaviour, indicating effective exchange coupling between FePt and Fe₃Pt. **b**, A nanocomposite from Fe₃O₄ (12 nm):Fe₅₈Pt₄₂ (4 nm) assembly. Owing to the phase separation in the 12 nm:4 nm assembly as illustrated in Fig. 1c, the annealed sample contained large body centred cubic (b.c.c.) Fe grains as confirmed by HRTEM and EDS, rendering a nanocomposite with the hysteresis showing two-phase behaviour. The kink at low field is related to the magnetization reversal of the soft Fe.

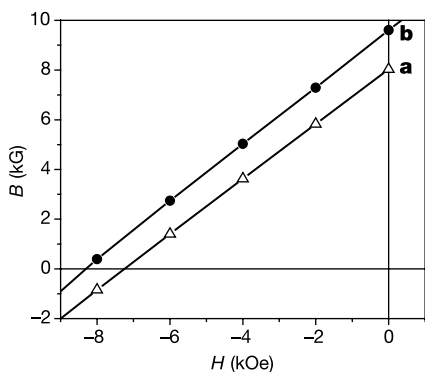


Figure 5 Second-quadrant B - H curves for the annealed samples. **a**, An annealed 4 nm $\text{Fe}_{58}\text{Pt}_{42}$ nanoparticle assembly. **b**, A hard-soft exchange-coupled FePt - Fe_3Pt nanocomposite. The composite was obtained from the annealed Fe_3O_4 (4 nm): $\text{Fe}_{58}\text{Pt}_{42}$ (4 nm) assembly (mass ratio Fe_3O_4 : FePt = 1:10). The energy product, $(BH)_{\text{max}}$, describes the available energy density of the materials and is defined as the maximum BH product of the second-quadrant B - H curve²¹.

The optimized nanostructures for exchange coupling yield both high remanent magnetization and coercivity, resulting in an enhanced energy product $(BH)_{\text{max}}$ (ref. 21). Figure 5 illustrates B - H curves of an annealed 4 nm $\text{Fe}_{58}\text{Pt}_{42}$ nanoparticle assembly (Fig. 5a), and a nanocomposite from a Fe_3O_4 (4 nm): $\text{Fe}_{58}\text{Pt}_{42}$ (4 nm) assembly with a 1:10 mass ratio (Fig. 5b). The measured $(BH)_{\text{max}}$ for the single-phase $\text{Fe}_{58}\text{Pt}_{42}$ is 14.7 MG Oe. For the nanocomposite derived from Fe_3O_4 (4 nm): $\text{Fe}_{58}\text{Pt}_{42}$ (4 nm) assembly, $(BH)_{\text{max}}$ reaches 20.1 MG Oe, exceeding the value for single phase $\text{Fe}_{58}\text{Pt}_{42}$ assembly by 37%, and the theoretical limit of 13 MG Oe for non-exchange-coupled isotropic FePt by over 50%. This $(BH)_{\text{max}}$ enhancement clearly indicates effective exchange coupling between the hard and soft phases.

We have described the fabrication of exchange-coupled isotropic FePt - Fe_3Pt nanocomposite magnets by self-assembly of binary FePt and Fe_3O_4 nanoparticles, and controlled annealing. By engineering the nanoscale dimension and spatial distribution of the hard and soft phases, an enhanced energy product is achieved. Our approach shows great potential for future fabrication of high-performance exchange-spring magnets. Further, it can be extended to other multi-component systems, providing both a model for studying fundamental relationships between nanostructure and interparticle interactions, and a practical route to functional nanocomposites and devices. □

Received 15 July; accepted 10 October 2002; doi:10.1038/nature01208.

1. Kneller, E. F. & Hawig, R. The exchange-spring magnet: a new material principle for permanent magnets. *IEEE Trans. Magn.* **27**, 3588–3600 (1991).
2. Skomski, R. & Coey, J. M. D. Giant energy product in nanostructured two-phase magnets. *Phys. Rev. B* **48**, 15812–15816 (1993).
3. Schrefl, T., Kronmüller, H. & Fidler, J. Exchange hardening in nano-structured two-phase permanent magnets. *J. Magn. Mater.* **127**, L273–L277 (1993).
4. Coehoorn, R., De Mooij, D. B. & De Waard, C. Melt-spun permanent magnet materials containing Fe_3B as the main phase. *J. Magn. Mater.* **80**, 101–104 (1989).
5. Ping, D. H., Hono, K. & Hirotsawa, S. Partitioning of Ga and Co atoms in a $\text{Fe}_3\text{B}/\text{Nd}_2\text{Fe}_{14}\text{B}$ nanocomposite magnet. *J. Appl. Phys.* **83**, 7769–7775 (1998).
6. Kobayashi, T., Yamasaki, M. & Hamano, M. Mössbauer study on intergranular phases in the bcc- Fe/NdFeB nanocomposite alloys. *J. Appl. Phys.* **87**, 6579–6581 (2000).
7. Gong, W., Hadjipanayis, G. C. & Krause, R. F. Mechanically alloyed nanocomposite magnets. *J. Appl. Phys.* **75**, 6649–6651 (1994).
8. McCormick, P. G. et al. Mechanically alloyed nanocomposite magnets. *J. Appl. Phys.* **83**, 6256–6261 (1998).
9. Zhang, J., Zhang, S.-Y., Zhang, H.-W., Shen, B.-G. & Li, B.-H. Structure and magnetic properties of $\text{Sm}_2\text{Co}_2/\alpha\text{-Fe}$ ($x = 0.65$ – 1.3) prepared by mechanical milling and subsequent annealing. *J. Appl. Phys.* **89**, 2857–2860 (2001).
10. Fullerton, E. E., Jiang, J. S., Sowers, C. H., Pearson, J. E. & Bader, S. D. Structure and magnetic properties of exchange-spring Sm-Co/Co superlattices. *Appl. Phys. Lett.* **72**, 380–382 (1997).
11. Liu, J. P., Luo, C. P., Liu, Y. & Sellmyer, D. J. High energy products in rapidly annealed nanoscale FePt multilayers. *Appl. Phys. Lett.* **72**, 483–485 (1998).

12. Liu, J. P., Liu, Y., Skomski, R. & Sellmyer, D. J. Magnetic hardening in SmCo_5 - Co multilayers and nanocomposites. *J. Appl. Phys.* **85**, 4812–4814 (1999).
13. Sun, S., Murray, C. B., Weller, D., Folks, L. & Moser, A. Monodisperse FePt nanoparticles and ferromagnetic FePt nanocrystal superlattices. *Science* **287**, 1989–1992 (2000).
14. Sun, S., Fullerton, E. E., Weller, D. & Murray, C. B. Compositionally controlled FePt nanoparticle materials. *IEEE Trans. Magn.* **37**, 1239–1243 (2001).
15. Sun, S. & Zeng, H. Size controlled synthesis of magnetite nanoparticles. *J. Am. Chem. Soc.* **124**, 8204–8205 (2002).
16. Kiely, C. J., Fink, J., Brust, M., Bethell, D. & Schiffrin, D. J. Spontaneous ordering of bimodal ensembles of nanoscopic gold clusters. *Nature* **396**, 444–446 (1998).
17. Weller, D. et al. High K_u materials approach to 100 Gbits/in². *IEEE Trans. Magn.* **36**, 10–15 (2000).
18. Klemmer, T., Hoydick, D., Okumura, H., Zhang, B. & Soffa, W. A. Magnetic hardening and coercivity mechanisms in L1_0 ordered FePd ferromagnets. *Scripta Met.* **33**, 1793–1805 (1995).
19. Podgorny, M. Electronic structure of the ordered phases of Pt-Fe alloys. *Phys. Rev. B* **43**, 13700–13718 (1991).
20. Zeng, H. et al. Exchange-coupled FePt nanoparticle assembly. *Appl. Phys. Lett.* **80**, 2583–2585 (2002).
21. O’Handley, R. C. *Modern Magnetic Materials* 469–472 (John Wiley & Sons, New York, 2000).

Acknowledgements This work is supported in part by the US Defense Advanced Research Program Agency (DARPA) through the Army Research Office (ARO). H. Z. and J. L. thank DARPA for support through Louisiana Tech University.

Competing interests statement The authors declare that they have no competing financial interests.

Correspondence and requests for materials should be addressed to S.S. (e-mail: ssun@us.ibm.com).

Active transport of Ca^{2+} by an artificial photosynthetic membrane

Ira M. Bennett*, Hebe M. Vanegas Farfano*, Federica Bogani*, Alex Primak*, Paul A. Liddell*, Luis Otero†, Leonides Sereno†, Juana J. Silber†, Ana L. Moore*, Thomas A. Moore* & Devens Gust*

* Department of Chemistry and Biochemistry and Center for the Study of Early Events in Photosynthesis, Arizona State University, Tempe, Arizona 85287, USA
 † Departamento de Química y Física, Universidad Nacional de Río Cuarto, Río Cuarto, Argentina

Transport of calcium ions across membranes and against a thermodynamic gradient is essential to many biological processes, including muscle contraction, the citric acid cycle, glycogen metabolism, release of neurotransmitters, vision, biological signal transduction and immune response. Synthetic systems that transport metal ions across lipid or liquid membranes are well known^{1–6}, and in some cases light has been used to facilitate transport⁷. Typically, a carrier molecule located in a symmetric membrane binds the ion from aqueous solution on one side and releases it on the other. The thermodynamic driving force is provided by an ion concentration difference between the two aqueous solutions, coupling to such a gradient in an auxiliary species, or photomodulation of the carrier by an asymmetric photon flux⁷. Here we report a different approach, in which active transport is driven not by concentration gradients, but by light-induced electron transfer in a photoactive molecule that is asymmetrically disposed across a lipid bilayer. The system comprises a synthetic, light-driven transmembrane Ca^{2+} pump based on a redox-sensitive, lipophilic Ca^{2+} -binding shuttle molecule whose function is powered by an intramembrane artificial photosynthetic reaction centre. The resulting structure transports calcium ions across the bilayer of a liposome to develop both a calcium ion concentration gradient and a membrane potential, expanding Mitchell’s concept of a redox loop mechanism for protons⁸ to include divalent cations. Although the quantum yield is relatively low (~ 1 per cent), the Ca^{2+} electrochemical potential developed is significant.